

Thermohaline-turbulence instability and thermohaline staircase formation in the polar oceans

Yuchen Ma * and W. R. Peltier*Department of Physics, University of Toronto, 60 St. George Street, Toronto M5S 1A7, Canada*

(Received 4 May 2022; accepted 11 July 2022; published 16 August 2022)

The Arctic Ocean's main thermocline may be characterized by a series of fine-scale thermohaline staircase structures that are present in a wide range of regions, the formation mechanism of which remains unclear. Recent analysis has led to the proposal of a theoretical model which suggested that these staircase structures form spontaneously in the ocean when the turbulent intensity determined by the buoyancy Reynolds number Re_b is sufficiently weak. In the current work, we have designed a series of Re_b controlled direct numerical simulations of turbulence in the Arctic Ocean thermocline to test the effectiveness of this theory. In these simulations, the staircases form naturally when Re_b falls in the range predicted by the instability criterion. The exponential growth rate of the layering mode matches well with the prediction of the theoretical model. The staircases formed in our simulations are further compared with the classical diffusive interface model, which argues that stable staircase structures can only form when the density ratio R_ρ is smaller than the critical value of $R_\rho^{cr} = \tau^{-1/2}$. Here τ is the ratio of haline diffusivity over thermal diffusivity. We show that the staircase structure can stably persist in our model regardless of whether or not $R_\rho < R_\rho^{cr}$ is satisfied.

DOI: [10.1103/PhysRevFluids.7.083801](https://doi.org/10.1103/PhysRevFluids.7.083801)

I. INTRODUCTION

Thermohaline staircases are strikingly organized structures in the oceans which are characterized by a series of vertically well-mixed layers of both heat and salt separated by sharp interfaces (see Chap. 8 of [1] for a recent review). Depending on whether the relatively warmer and saltier waters are lying above or below the relatively colder and fresher waters, the thermohaline staircases can be classified into salt-fingering staircases which are usually observed in low- and mid-latitude oceans (e.g., [2,3]) and the diffusive-convection staircases which are mainly observed in the polar oceans (e.g., [4,5]). The first observations of these two types of thermohaline staircases were reported in the late 1960s [6,7] and their origins were quickly connected with the two types of double-diffusive convection: salt fingering and diffusive convection. However, half a century later, we are only “halfway” towards a complete understanding of their formation mechanisms. While we have already gained the ground-breaking understanding of the detailed mechanism for the salt-fingering staircases, it is still unclear what the key mechanism is that is responsible for the formation of the diffusive-convection staircases.

On the salt-fingering side of the story, the formation of the staircases has been explained using the instability of the flux-gradient laws, initially discussed in [8]. In this work, the author used the

*Corresponding author: yc.ma@mail.utoronto.ca

parametrized diapycnal diffusivities for heat, K_Θ , and salt, K_S , to describe the large-scale effect of the stochastic field of salt fingers and assumed that K_Θ and K_S are determined solely on the density ratio $R_\rho^{SF} \equiv \Theta_z/S_z$ (here Θ and S are the potential temperature field and salinity, both in density units). Following this assumption, the author analyzed the linear stability of the parametrized mean-field model and derived the criterion for the layering instability. The dependence of K_Θ and K_S on R_ρ^{SF} has been calibrated using direct numerical simulations (DNSs) (e.g., [9–12]) and accumulating evidence has established that layers will spontaneously form from homogeneous salt-fingering fields once this criterion is satisfied, which includes DNSs (e.g., [13]), basin-scale model simulation (e.g., [14]), and mean-field model simulations (e.g., [15–17]). Most importantly, the multiscale version of the flux-gradient model proposed in [16] successfully solved the ultraviolet catastrophe problem that existed in the original theoretical framework of [8]. The growth rate of the instability in this new model is shown to decrease to a very small value after R_ρ reaches the value of 1.8, which perfectly explains why nearly all the salt-fingering staircases observed in the ocean have the density ratio R_ρ^{SF} smaller than 2 (see [18] or [1] for a review).

The above theory for salt-fingering staircase formation suggests that the salt-fingering fluxes formed from salt-fingering instability are sufficient to drive the system into a layered state. However, this simple picture does not suffice to provide an explanation of staircase formation in the diffusive-convection regime. While most diffusive-convection staircases have been found to exist in a large range of density ratio $2 < R_\rho < 9$ (see [5,19], for example; here $R_\rho \equiv S_z/\Theta_z$ is the density ratio for the diffusive convection system), the linear diffusive-convection instability is only active in a tiny window of the parameter space $1 < R_\rho < 1.16$ (see [1]). This mismatch strongly suggests that the linear diffusive-convection instability cannot be regarded as the origin of diffusive-convection staircases, for example, that are observed in the Arctic Ocean. At least another critical element has to be introduced to “react” with the diffusive convection to explain the observations. One of the most promising candidates for the explanation has been that associated with thermohaline-shear instability theory initially proposed in [20], and in this case this critical element is “shear.” In this work and the following work of [21,22], it is demonstrated that a flow that is stable to both shear instability and diffusive-convection instability might become unstable under the joint action of diffusive convection and different forms of shear. It has been further shown that these instabilities are able to develop into layered structures in the nonlinear evolution of DNSs [20]. While the thermohaline-shear instability perfectly solves the problem of the mismatch between the different ranges of density ratio, the development for the instability is still currently dependent on some specific form of the shear (e.g., a vertically sinusoidal form is considered in [20] and the time-dependent form is considered in [21,22]). Another candidate explanation for the diffusive-convection staircases is the thermohaline intrusion mechanism discussed in [23,24] where the critical element added to the picture is the “horizontal gradient.” This theory was first discussed to explain the formation of salt-fingering staircases in [23] and it was extended to explain the diffusive-convection staircases in [24]. While the coexistence of thermohaline intrusion and double-diffusive staircases are often apparent in the observational data as shown in [24], it remains a challenging question as to whether the presence of horizontal gradients is a necessary condition for staircases to form in the diffusive-convection regime, considering that salt-fingering staircases have now been shown to be able to form without horizontal gradients (e.g., [8]).

While these two candidate theories described above may significantly contribute to our understanding of the problem, we believe that a more general theory should exist for the formation of diffusive-convection staircases which is also based on the instability of certain flux-gradient laws. Recently, such a new theory for the formation of staircases in the diffusive-convection regime was proposed in [25] (hereafter referred to as MP21), in which the critical element added to the picture is the “stratified turbulence.” In this paper the effective turbulent diapycnal diffusivities for heat, K_Θ , and salt, K_S , in the diffusive-convection regime are parametrized as being solely dependent upon the buoyancy Reynolds number $Re_b = \epsilon/(\nu N^2)$ (here ν is the kinematic viscosity, ϵ is the viscous dissipation rate, and $N = \sqrt{-g/\rho_0 \langle d\bar{\rho}/dz \rangle}$ is the buoyancy frequency). By analyzing the linear stability of the parametrized mean-field model and assuming the specific functional

dependence of $K_\Theta(\text{Re}_b)$ and $K_S(\text{Re}_b)$ described in [26], MP21 demonstrated that the system will be susceptible to layering instability if the turbulence intensity characterized by the buoyancy Reynolds number is at an intermediate level. The key idea that underlies this theory is that the formation of the diffusive-convection staircases originates from the background stratified turbulence instead of diffusive-convection instability. One mechanism that leads to layer formation from stratified turbulence is the “Phillips mechanism” previously proposed in [27], which was extended most recently in [28]. These analyses apply to a fluid in which density is determined by only a single advecting and diffusing species. Since Arctic Ocean staircases involve perfectly correlated steps in both temperature and salinity it is clear that no analysis based upon the assumption of a single component fluid can suffice to solve to the problem. Nevertheless, as explicitly discussed in MP21, the Phillips mechanism for the staircase in the salinity component of Arctic staircases is “lurking” in the background of the results for the two-component system. Because the theory described in MP21 is based on stratified turbulence parametrization that involves both temperature and salinity, we will refer to this theory as the thermohaline-turbulence instability theory in what follows for simplicity.

There are three lines of evidence that strongly support the thermohaline-turbulence instability theory as a highly plausible mechanism for the formation of staircase structures in the diffusive convection environment. First, the critical assumption employed in MP21 that K_Θ and K_S can be parametrized based on the parametrization scheme in [26] is confirmed to be highly accurate by the DNSs of Kelvin-Helmholtz engendered turbulence simulations of [29]. Second, the mean-field model simulation performed in MP21 confirmed that the initially fastest growing mode developed from the thermohaline-turbulence instability mechanism does grow into the layered state in the nonlinear stage of evolution. Third, the criterion in MP21, which states that the formation mechanism is strongly determined by Re_b and weakly dependent on R_ρ , is consistent with a series of oceanographic measurements (e.g., [19,30]), as discussed in detail in MP21.

Despite the supporting evidence there remain two critical questions upon which we will focus in the present paper. First, we will test whether the development of the thermohaline-turbulence instability will inevitably lead to the formation of a thermohaline staircase structure in a DNS of a three-dimensional fully developed turbulent flow. It needs to be kept in mind that the current form of thermohaline-turbulence instability theory described in MP21 is a linear stability theory that relies on a series of idealized assumptions. Therefore it is crucial for us to evaluate its effectiveness using simulations that resolve the smallest scales of fluid dynamics. Second, we want to understand whether the thermohaline staircases formed from the thermohaline-turbulence instability will remain as stable structures and what mechanism is responsible for keeping such interfaces robust. In the early literature a comprehensive theoretical analysis of the diffusive interfaces was developed in [31], hereafter LS. The model developed in LS has been widely used as the basis for the analyses on the diffusive interface structure by researchers in this field (e.g., [32,33]). An important prediction of LS’s theory is that no steady interface structure can exist when $R_\rho > \tau^{-1/2}$ ($\tau = \kappa_s/\kappa_\theta$ is the ratio of molecular diffusivities for salt and heat; $\tau^{-1/2} \approx 10$ in the Arctic Ocean). In contrast, the thermohaline-turbulence instability theory predicts that the system can be unstable to the layering mode at any R_ρ that is larger than 1. Therefore, the second major goal of this paper is to explore the conditions under which stable staircase structure can persist in our DNSs and compare them with the classical theory of LS. It should be noticed that although most of the diffusive interfaces have been found in regions with $R_\rho < 10$ in the measurements of ocean and lakes (see review of [34], for example), observed diffusive staircases with $R_\rho > 10$ do exist occasionally (e.g., [35,36]).

In addressing this paper’s primary goals, we will conduct a series of body-forced DNSs driven by the stochastic forcing of large-scale vortical modes. Vortical mode body forcing has been implemented in previous work to study homogenous stratified turbulence (e.g., [37–40]). It is well suited for the exploration of layer formation occurring through thermohaline-turbulence instability since it allows us to properly control the energy input into the system that is required to control the averaged Re_b of the system. As we will demonstrate in what follows, if and only if the averaged Re_b lies in the unstable regime predicted by MP21 will the system develop into a layered state.

The remainder of the paper will be arranged as follows. In Sec. II we will briefly review the derivation of the thermohaline-turbulence instability theory. The settings of the DNSs employed in this work will be presented in Sec. III. In Sec. IV we will describe the time evolution of the system and illustrate how the layered structure forms in the system. These simulation results will be analyzed and compared with the theoretical prediction of MP21 in various different ways. In Sec. V we will analyze the interface structure formed in our numerical system in detail to illustrate how the stable staircase state is maintained and compare it with the classical theory of LS. Finally we summarize our conclusions in Sec. VI.

II. SUMMARY OF THERMOHALINE-TURBULENCE INSTABILITY THEORY

In this section, we will briefly review the original formulation of the thermohaline-turbulence instability theory discussed in MP21 in order to provide context for the discussion to follow that begins in section 3.

The theory of MP21 considers the evolution of the stratified turbulence that develops in a background state in which the stratifications of temperature and salinity lie in the diffusive-convection regime. In this circumstance it is assumed that the average effect of microscale stratified turbulence on the larger scale background can be adequately captured by the effective turbulent diapycnal diffusivities for temperature, K_Θ , and salinity, K_S . It is then further assumed that both K_Θ and K_S are only dependent upon the buoyancy Reynolds number Re_b of the system so that the governing mean-field equations for the one-dimensional averaged temperature profile $\Theta(z, t)$ and salinity profile $S(z, t)$ have the forms

$$\begin{aligned}\frac{\partial \Theta}{\partial t} &= -\frac{\partial}{\partial z} F_\Theta = \frac{\partial}{\partial z} \left(K_\Theta(\text{Re}_b) \frac{\partial \Theta}{\partial z} \right), \\ \frac{\partial S}{\partial t} &= -\frac{\partial}{\partial z} F_S = \frac{\partial}{\partial z} \left(K_S(\text{Re}_b) \frac{\partial S}{\partial z} \right).\end{aligned}\quad (1)$$

In the above equations, Θ and S are defined in density units so that the equation of state can be written as $\rho = \rho_0 + S - \Theta$. The system is initialized with uniform gradients $\overline{\Theta}(z, t = 0) = -\Theta_{z0}z$ and $\overline{S}(z, t = 0) = -S_{z0}z$ (here $\Theta_{z0} > 0$ and $S_{z0} > 0$), which determines a background density ratio $R_\rho = S_{z0}/\Theta_{z0}$. $\Theta(z)$ and $S(z)$ at later times are decomposed into a combination of background fields $\overline{\Theta} = -\Theta_{z0}z$, $\overline{S} = -S_{z0}z$ and weak perturbations Θ', S' , as

$$\Theta(z) = \overline{\Theta}(z) + \Theta'(z), \quad S(z) = \overline{S}(z) + S'(z). \quad (2)$$

These perturbations $\Theta'(z)$ and $S'(z)$ will then lead to a variation of $\text{Re}_b(z)$ by the amount

$$\text{Re}'_b(z) = \frac{\partial \text{Re}_b}{\partial \rho_z} \frac{\partial \rho'}{\partial z} = -\frac{\rho_0}{\nu g} \frac{\epsilon_0}{\frac{\partial \overline{\rho}}{\partial z}} \frac{\frac{\partial \rho'}{\partial z}}{\frac{\partial \overline{\rho}}{\partial z}} \equiv -\overline{\text{Re}}_b \frac{\frac{\partial S'}{\partial z} - \frac{\partial \Theta'}{\partial z}}{\frac{\partial \overline{\rho}}{\partial z}}. \quad (3)$$

In the above equation, the viscous dissipation ϵ_0 in the system is assumed to be a constant which determines the background buoyancy Reynolds number of the system, $\overline{\text{Re}}_b$. $\text{Re}'_b(z)$ feeds back on the time evolution of $\Theta(z)$ and $S(z)$ through the governing equations (1). Positive feedback for certain modes will lead to the general instability of the system. By expanding the perturbations in normal modes $(\Theta', S') = (\hat{\Theta}, \hat{S}) \exp(\lambda t) \exp(ikz)$ and keeping only the first-order terms, the original equation set (1) will be transformed to an eigenvalue problem with the growth rate λ as the eigenvalue of the resulting 2×2 matrix. The value of λ is then determined by solving the quadratic equation resulting in

$$\begin{aligned}\lambda^2 + k^2 \left(K_\Theta + K_S + \frac{\partial K_S}{\partial \text{Re}_b} \Big|_{\overline{\text{Re}}_b} \frac{\overline{\text{Re}}_b R_\rho}{R_\rho - 1} - \frac{\partial K_\Theta}{\partial \text{Re}_b} \Big|_{\overline{\text{Re}}_b} \frac{\overline{\text{Re}}_b}{R_\rho - 1} \right) \lambda \\ + k^4 \left(K_\Theta K_S + \frac{\partial K_\Theta}{\partial \text{Re}_b} \Big|_{\overline{\text{Re}}_b} K_S \overline{\text{Re}}_b \frac{1}{R_\rho - 1} - \frac{\partial K_S}{\partial \text{Re}_b} \Big|_{\overline{\text{Re}}_b} K_\Theta \overline{\text{Re}}_b \frac{R_\rho}{R_\rho - 1} \right) = 0.\end{aligned}\quad (4)$$

A positive value of λ , which represents instability of the system, will be obtained if and only if the following criterion is satisfied:

$$K_{\ominus} K_S + \left. \frac{\partial K_{\ominus}}{\partial \text{Re}_b} \right|_{\overline{\text{Re}_b}} K_S \overline{\text{Re}_b} \frac{1}{R_{\rho} - 1} - \left. \frac{\partial K_S}{\partial \text{Re}_b} \right|_{\overline{\text{Re}_b}} K_{\ominus} \overline{\text{Re}_b} \frac{R_{\rho}}{R_{\rho} - 1} < 0. \quad (5)$$

If we assume that K_S and K_{\ominus} have a local power law dependence on Re_b as $K_S \sim \text{Re}_b^{\beta_s}$ and $K_{\ominus} \sim \text{Re}_b^{\beta_{\theta}}$, the above criterion will be simplified to

$$\beta_s - 1 > \frac{\beta_{\theta} - 1}{R_{\rho}}. \quad (6)$$

Therefore the precise criterion for the instability depends on the details of the parametrization scheme employed to describe the dependence of the turbulent diffusivities upon the buoyancy Reynolds number in the stratified turbulent flow. Parameterization of the diapycnal diffusivities (or mixing efficiency) of stratified turbulence has remained a significant scientific challenge. Various forms of such turbulence parametrization have been proposed based on different combinations of nondimensional parameters in the past two decades. The list of these contributions would include [41], which proposed a parametrization of diapycnal diffusivities that was solely based on Re_b ; in [42] a multiparameter parametrization was discussed that depends on Re_b and gradient Richardson number Ri . In [39] it was found that at large Re_b the mixing efficiency is sensitive to horizontal Froude number Fr . Although all these parametrization schemes highlight some aspects of the turbulent mixing, that in the Arctic Ocean is special in the sense that it is weak energetically so that the diapycnal diffusivities for heat and salt become dramatically different due to their different values of molecular diffusivity (see, e.g., [43]). To take this effect into account, the parametrization scheme employed in the Arctic Ocean environment must depend explicitly on the molecular Prandtl number Pr . To our knowledge, the only parametrization that explicitly discusses the dependence on Pr comes from the work of [26]. In MP21 we employed the empirically calibrated parametrization scheme for single-component fluids of [26] as the candidate parametrization. This is based on the somewhat bold assumption that the temperature and salinity field will be relatively independent in the state and therefore this pair of single-component parametrizations should provide an accurate description of the doubly diffusive turbulent system. The effectiveness of this description has been confirmed in our recent work [29] and it will also be tested in the current numerical model in Sec. IV B below. The specific functional form of the parametrization scheme of [26] is as follows:

$$K_{\rho}^{BB}(\text{Re}_b, \text{Pr}) = \begin{cases} \kappa & \text{if } \text{Re}_b < 10^{\frac{2}{3}} \text{Pr}^{-\frac{1}{2}} \\ \frac{0.1}{\text{Pr}^{\frac{1}{4}}} \nu \text{Re}_b^{\frac{3}{2}} & \text{if } 10^{\frac{2}{3}} \text{Pr}^{-\frac{1}{2}} < \text{Re}_b < (3 \ln \sqrt{\text{Pr}})^2 \\ 0.2 \nu \text{Re}_b & \text{if } (3 \ln \sqrt{\text{Pr}})^2 < \text{Re}_b < 100 \\ 2 \nu \text{Re}_b^{\frac{1}{2}} & \text{if } \text{Re}_b > 100. \end{cases} \quad (7)$$

If we substitute $\text{Pr} = 700$ and $\text{Pr} = 7$ (typical Prandtl values for salinity and temperature in seawater) into the above equations to obtain the forms of $K_S(\text{Re}_b)$ and $K_{\ominus}(\text{Re}_b)$, respectively, the criterion described in Eq. (6) can be evaluated to obtain the following condition:

$$0.17 < \overline{\text{Re}_b} < 97. \quad (8)$$

Once this criterion is satisfied, the layering mode of instability will continually grow until diffusive-convection staircases form, as demonstrated by the nonlinear mean-field model simulation in MP21. However, as will be discussed in detail in what follows, we will employ a smaller value of Schmidt number (Prandtl number for salinity), $\text{Sc} = 70$, for salinity in the DNSs to be discussed herein due to the constraints on computational resources. In this circumstance, Eq. (7) gives a different formula for the salinity diffusivities which will lead to a revised $\overline{\text{Re}_b}$ criterion of

$$0.55 < \overline{\text{Re}_b} < 41. \quad (9)$$

While Eq. (8) is still the criterion that should be applied to the real oceanographic environment (upper-bound and lower-bound values may change slightly in regions where Schmidt number deviates from 700), the effectiveness of the theory should be tested based on criterion (9) under the choice of parameters in our DNSs.

III. DIRECT NUMERICAL SIMULATIONS

In this section we discuss the design of DNS analyses to be employed to study the development of the layering structures that form from the thermohaline-turbulence instability. In what follows, we will first discuss the governing equations and critical physical quantities in Sec. III A. Then, in Sec. III B we will discuss the detailed numerical settings of our DNSs.

A. Governing equations and physical quantities

In order to develop a state of homogeneous stratified turbulence in the diffusive-convection regime, we consider the temperature $\Theta(x, y, z, t)$ and salinity $S(x, y, z, t)$ fields that are composed of background temperature and salinity fields characterized by negative vertical gradients $-\Theta_{z0}$ and $-S_{z0}$ and perturbation fields $\Theta^{pt}(x, y, z, t)$ and $S^{pt}(x, y, z, t)$, namely,

$$\begin{aligned}\Theta(x, y, z, t) &= -\Theta_{z0}z + \Theta^{pt}(x, y, z, t), \\ S(x, y, z, t) &= -S_{z0}z + S^{pt}(x, y, z, t).\end{aligned}\tag{10}$$

Subject to the Boussinesq approximation, the scalar fields $\Theta^{pt}(x, y, z, t)$, $S^{pt}(x, y, z, t)$ and the velocity field $\mathbf{u}(x, y, z, t) = (u(x, y, z, t), v(x, y, z, t), w(x, y, z, t))$ are governed by the Navier-Stokes equations as in

$$\begin{aligned}\frac{\partial \mathbf{u}}{\partial t} + \mathbf{u} \cdot \nabla \mathbf{u} &= -\nabla p - J \left(\frac{R_\rho}{R_\rho - 1} S^{pt} - \frac{1}{R_\rho - 1} \Theta^{pt} \right) \mathbf{e}_z + \frac{1}{\text{Re}} \nabla^2 \mathbf{u} + \mathbf{F}, \\ \nabla \cdot \mathbf{u} &= 0, \\ \frac{\partial \Theta^{pt}}{\partial t} + \mathbf{u} \cdot \nabla \Theta^{pt} &= \frac{1}{\text{RePr}} \nabla^2 \Theta^{pt} + w, \\ \frac{\partial S^{pt}}{\partial t} + \mathbf{u} \cdot \nabla S^{pt} &= \frac{1}{\text{ReSc}} \nabla^2 S^{pt} + w.\end{aligned}\tag{11}$$

In the above equations, \mathbf{e}_z is the unit vector in the positive vertical direction. The “+w” terms on the right-hand side of the latter two equations come from the vertical advection of the background vertical gradients $-\Theta_{z0}$ and $-S_{z0}$. We have nondimensionalized the above equations using the length scale L_0 , velocity scale U_0 , temperature scale $\Delta\Theta = \Theta_{z0}L_0$, salinity scale $\Delta S = S_{z0}L_0$, and density scale $\Delta\rho = \Delta S - \Delta\Theta$. Here L_0 and U_0 are characteristic scales of the shear modes we employ to initialize the system, which will be discussed in detail in the next section.

The critical nondimensional parameters are the Reynolds number Re , bulk Richardson number J , inverse density ratio R_ρ , Prandtl number Pr , and Schmidt number Sc , which can then be defined explicitly as

$$\text{Re} = \frac{U_0 L_0}{\nu}, \quad J = \frac{g \Delta \rho L_0}{\rho_0 U_0^2}, \quad R_\rho = \frac{\Delta S}{\Delta \Theta}, \quad \text{Pr} = \frac{\nu}{\kappa_\theta}, \quad \text{Sc} = \frac{\nu}{\kappa_s},\tag{12}$$

where ν is the kinematic viscosity, κ_θ and κ_s are molecular diffusivities for heat and salt, and ρ_0 is the reference density. We also assume that the system is subject to an external body forcing \mathbf{F} whose specific form will be discussed in detail in the next section.

Based on Eqs. (11), we can straightforwardly derive the time derivative of the volume-averaged kinetic energy of the system $K_{\text{lin}} \equiv 1/2 \langle |\mathbf{u}|^2 \rangle$ as (here and below $\langle \cdot \rangle$ represents the volume averages):

$$\frac{dK_{\text{lin}}}{dt} = P - (F_{b\theta} + F_{bs}) - \epsilon,\tag{13}$$

where

$$P = \langle \mathbf{u} \cdot \mathbf{F} \rangle, \quad \epsilon = \frac{2}{\text{Re}} \langle s_{ij} s_{ij} \rangle, \quad F_{b\theta} = -\frac{J}{R_\rho - 1} \langle w' \Theta' \rangle, \quad F_{bs} = \frac{J R_\rho}{R_\rho - 1} \langle w' S' \rangle \quad (14)$$

are defined to be the energy input from external forcing, viscous dissipation ratio, and buoyancy flux associated with temperature and salinity, respectively. $s_{ij} = 1/2(\partial u_i/\partial x_j + \partial u_j/\partial x_i)$ is the strain rate tensor. In the last two equations and in the rest of the paper, we decomposed a given field $f(x, y, z, t)$ into $f = \bar{f} + f'$ so that \bar{f} represents the horizontal average of that field (except for $\overline{\text{Re}_b}$ which represents the background buoyancy Reynolds number as will be introduced below) and f' represents perturbation to it. It should be noticed that the unstably stratified background temperature field continues to release energy to the system through the heat flux ($F_{b\theta} < 0$); meanwhile the energy of the system continues to be invested in mixing the stably stratified salinity gradient through the salt flux ($F_{bs} > 0$).

When the system remains in a quasisteady state, the right-hand side of Eq. (13) should be approximately zero. Considering that the absolute value of buoyancy fluxes $F_{b\theta}$ and F_{bs} are usually much smaller than the viscous dissipation ϵ in our system (as will be demonstrated below), the balance of the K_{in} budget is mainly kept by the first and last terms of the right-hand side of Eq. (13), namely,

$$P \sim \epsilon. \quad (15)$$

The background buoyancy Reynolds number $\overline{\text{Re}_b}$, which is controlled directly by ϵ , can then be estimated through

$$\overline{\text{Re}_b} \equiv \frac{\text{Re}}{J} \epsilon \sim \frac{\text{Re}}{J} P. \quad (16)$$

By controlling the energy input rate P , we can control the value of $\overline{\text{Re}_b}$ of the system. This allows us to test our criterion for staircase formation in thermohaline-turbulence instability theory which is based solely on $\overline{\text{Re}_b}$.

B. Numerical methods

Governing equations (11) are integrated in a triply periodic cubic domain of length 2π using the open-source computational fluid dynamics software NEK5000 [44]. NEK5000 was developed at Argonne National Laboratory based on the spectral element method (e.g., [45,46]) which is a useful tool for simulating transitional and turbulent flow.

For the system to achieve a quasisteady state, we choose to apply very similar initial fields and forcing with the settings of the recent body-forced simulations [40]. Specifically the initial fields are defined as a superposition of randomly phased horizontal shear modes $\mathbf{u}_{\text{shear}}$ and randomly phased three-dimensional internal wave modes ($\mathbf{u}_{\text{internal}}, \Theta_{\text{internal}}, S_{\text{internal}}$). The shear modes are confined to large-scale modes $m \leq m_c = 7$ only and the amplitude for a mode with vertical wavenumber m is allocated to be proportional to $1/m$ in order to follow the initial energy spectrum of m^{-2} . The detailed functional form of $\mathbf{u}_{\text{shear}}$ is as follows:

$$(u_{\text{shear}}, v_{\text{shear}}, 0) = \frac{1}{\sqrt{m_c}} \sum_{m=1}^{m_c} \frac{1}{m} (\cos(\phi_m + mz), \sin(\phi_m + mz), 0), \quad (17)$$

where ϕ_m is the phase chosen randomly for each vertical mode. It should be noticed that these shear modes have been nondimensionalized by their characteristic velocity scale U_0 and length scale L_0 , in such a way that the velocity amplitude of these shear modes has a nondimensional scale of $O(1)$ and the volume-averaged nondimensional squared shear $\langle S^2 \rangle = \langle (\partial u_{\text{shear}}/\partial z)^2 + (\partial v_{\text{shear}}/\partial z)^2 \rangle$ is equal to 1. The form of the internal wave modes ($\mathbf{u}_{\text{internal}}, \Theta_{\text{internal}}, S_{\text{internal}}$), on the other hand, is initialized based upon the algorithm discussed in Appendix B of [47] to satisfy the three-dimensional Garrett-Munk spectrum. These internal wave modes contribute 10% of the initial energy and they are only

TABLE I. Governing parameters for the direct numerical simulations performed in this paper.

No.	L_z	P	R_ρ	Pr	Sc	Re	J
1	2π	0.01	2	7	70	1000	1
2	2π	0.01	5	7	70	1000	1
3	2π	0.01	8	7	70	1000	1
4	2π	0.01	∞	N.A.	70	1000	1
5	2π	0.1	2	7	70	1000	1
6	4π	0.01	5	7	70	1000	1

nonzero for modes with $|\mathbf{k}| \leq 7$. For recent discussions of the Garrett-Munk spectrum of internal waves in the oceans and the ability of high-resolution ocean models forced by both the atmosphere and the astronomical tidal potential to replicate this spectrum see [48,49].

We first integrate the system without body forcing to 20 time units in order for the energy contained in the initial larger scale modes to cascade to the small scales, a strategy previously employed in [40]. Then we begin to introduce body forcing with an appropriate form to represent the stochastic forcing of the large-scale modes. As employed in previous DNSs (e.g., [38–40]), these vortical modes of forcing only act on the horizontal component of the velocity and can be written in the following form:

$$(F_x, F_y) = A \sum_{(k,l)} A_{k,l}(l, -k)e^{i(kx+ly)}, \quad (18)$$

where k and l are the wavenumbers in the x and y directions, respectively. The forcing is only nonzero for modes whose horizontal wavenumber $k_h = \sqrt{k^2 + l^2}$ lies in the small parameter window of $2.5 \leq k_h \leq 3.5$, as optimized in [40]. The complex action for each mode $A_{k,l}$ is chosen randomly at each time step, after which a normalization constant A is determined so as to control the energy input rate P at each time step to be a constant (we used the method proposed in [39] to avoid accidental energy inputs due to the finite time steps).

We have performed six different simulations that will be discussed in this paper, whose governing parameters are summarized in Table I. While fixed values of $\text{Re} = 1000$, $J = 1$, $\text{Pr} = 7$, and $\text{Sc} = 70$ were employed for all these simulations, we vary the density ratio R_ρ for simulations 1–4 to investigate how R_ρ will influence the dynamics of the system’s equilibrium state. It will be important to note that $R_\rho \rightarrow \infty$ for simulation 4 is achieved by integrating the system in the single-component stratification case with $\text{Sc} = 70$. In these simulations, we set the energy-input rate $P = 0.01$ so that the $\overline{\text{Re}_b} \sim 10$ of each simulation is within instability criterion (9). For control simulation 5, we switched P to the value 0.1 which leads to a larger value of $\overline{\text{Re}_b} \sim 100$ that is well beyond the upper limit of the instability criterion. We could not afford to test our theory for $\overline{\text{Re}_b} \ll 10$ by making simulations with $P \ll 0.01$ because the layering mode is predicted to grow too slowly for small $\overline{\text{Re}_b}$ to be verified in the numerical simulations. For control experiment 6, we double the vertical extent of the domain with $R_\rho = 5$ to investigate how the layer formation process is dependent upon this characteristic of the model.

For simulations 1–5 in this paper, we first apply an intermediate resolution of $350 \times 350 \times 350$ grid points in the simulation domain (for simulation 6, in which the vertical domain is doubled, the vertical resolution is always doubled for consistency). From a theoretical perspective this resolution cannot reach the requirement of DNS as the mesh could not reach the Batchelor’s scale for the slower diffusing salinity. However, in order to represent the layer formation process, both the large domain size and the long integration time are necessary for our simulations, which restricts the resolution that can be applied. In the Appendix, we compared simulations with different resolutions to show that the layer formation we report in this paper is resolution independent. Once the steady layered structure forms in the numerical simulations (the corresponding time is marked as $t = t_1$),

we then double the resolution in each direction to $700 \times 700 \times 700$ grid points for simulations 1–5, which allows us to better resolve the structure of the staircase state that forms. This system is then integrated for a short time until the system stabilizes again at $t = t_2$. In what follows, we will first analyze the layer formation process characterized by the long integration of intermediate resolution in Sec. IV. Then we will analyze the staircase states in detail by focusing on the subsequent high-resolution evolution to be discussed in Sec. V.

IV. SPONTANEOUS FORMATION OF THERMOHALINE STAIRCASES IN THE DIRECT NUMERICAL SIMULATIONS

In this section, we will focus on discussing the process of spontaneous formation of layered structures in our system. In Sec. IV A we will first describe the layer formation process in simulations with different $\overline{\text{Re}}_b$ and R_ρ . Then in Sec. IV B we will provide a detailed comparison between the layer formation rate in the simulations and the linear growth rate derived from Sec. II. By doing this, we will be able to evaluate whether the thermohaline-turbulence instability theory is indeed dominating the nonlinear evolution process of our DNSs. The discussion in this section is confined to the layer-formation phase of the evolution that is characterized by time $t \leq t_1$.

A. Thermohaline layering state in the direct numerical simulations

In our simulations, well-defined layered structures form spontaneously in all simulations except for simulation 5 in which a stronger forcing is applied. As an example, the layer formation process for simulation 1 is illustrated in Fig. 1, in which we show the state of the temperature and salinity fields in pseudocolor plots [Figs. 1(a)–1(f)] and the horizontally averaged vertical profiles [Figs. 1(g)–1(i)]. At $t = 100$ [Figs. 1(a), 1(d), and 1(g)], the constant energy input from the vortical modes keeps the system in a homogeneously stratified turbulent state in which the temperature and salinity fields remain in the linear-gradient configuration. After a long integration time, the first sign of the formation of the vertical structure occurs at approximately $t_i = 1000$ (t_i represents the time that the initial layered structure forms). As shown in Figs. 1(b), 1(e), and 1(h), the system develops into a four-step staircase state at this time of its evolution. These four-step staircases then gradually merge to form a well-defined two-step layered state at approximately $t_m = 2100$ (t_m represents the time that the layers merge into higher steps in our system), which is then retained in the system until the end of the simulation at $t_1 = 3098$. The layered state at $t = t_1$ is illustrated in Figs. 1(c), 1(f), and 1(i). By comparing Figs. 1(h) and 1(i), we can notice that the merged two-layer state has much sharper interfaces and more homogenized mixed layers than the four-layer state. In what follows, we will use the phrase “staggered layered state” to describe the layered state that is not very well shaped, as in Fig. 1(h).

These different phases of the layer formation process can also be viewed in the time variation of $F_{b\theta}$ and F_{bs} depicted in Fig. 2. In this figure, three different phases, namely, the initial staircase formation stage, layer merging stage, and equilibrium stage, are separated by three characteristic times (t_i , t_m , t_1) which are denoted using the vertical lines. Generally speaking, both $|F_{b\theta}|$ and $|F_{bs}|$ experience a continuous increase during the layer formation stage and layer merging stage until they become stabilized in the final equilibrium stage of evolution. This trend of increasing $|F_{b\theta}|$, $|F_{bs}|$ as layers form and merge is consistent with previous numerical simulations of thermohaline staircases of the salt-fingering system [13] and the low-Pr diffusive-convection system [50]. Meanwhile, the net buoyancy flux $F_b = |F_{bs}| - |F_{b\theta}|$ keeps decreasing from positive values to negative values in the entire evolution process. As we will discuss in the next section, this increase of energy flow to the kinetic energy reservoir will increase viscous dissipation in the system.

The above-described evolution process generally applies also for simulations 2–4 (whose R_ρ is changed to $R_\rho = 5$, $R_\rho = 8$, and $R_\rho = \infty$, respectively). In these simulations, however, the first formed staggered layered state has two steps, which then merge into the single-step layered state and the mixed layer occupies almost the entire domain. An example of such evolution can be seen in

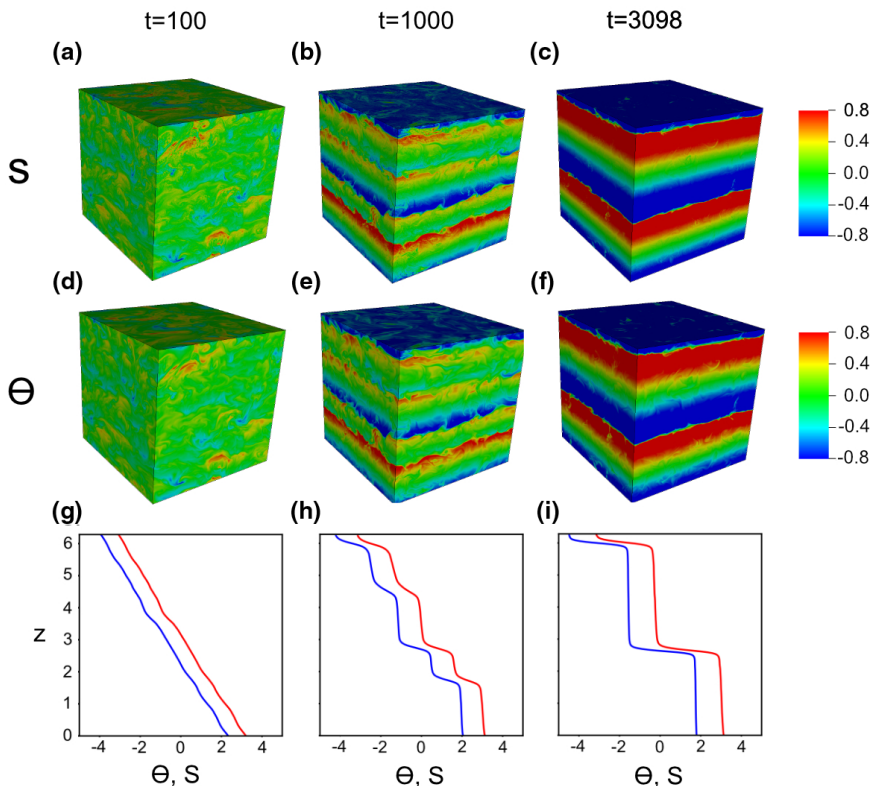


FIG. 1. The pseudocolor plots of (a–c) the salinity field $S^p(x, y, z, t)$ and (d–f) the temperature field $\Theta^p(x, y, z, t)$ at three different time slices $t = 100$, $t = t_i = 1000$, and $t = t_i = 3098$ for simulation 1. (g–i) The horizontally averaged profiles of salinity $\bar{S}(z)$ (blue) and temperature $\bar{\Theta}(z)$ (red) as a function of depth for the same time slices.

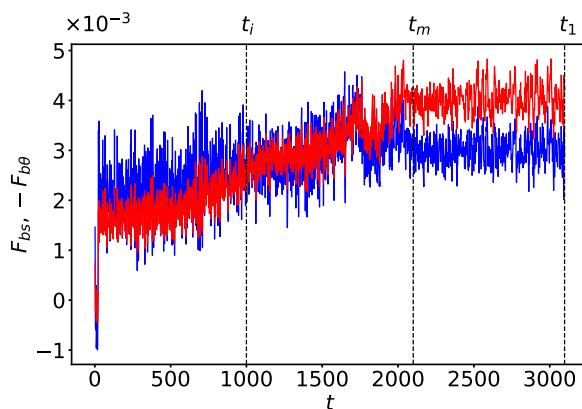


FIG. 2. Evolution of the temperature-induced buoyancy flux $F_{b\theta}$ (red) and salinity-induced buoyancy flux F_{bs} (blue) in the evolution of simulation 1. Temperature-induced buoyancy flux is plotted with the absolute (negative) value for comparison. The three characteristic times t_i , t_m , and t_1 represent the time that the first layered structure forms, the time that layers merge into higher steps, and the end of the intermediate resolution simulation, respectively (their definitions are discussed in detail in the text).

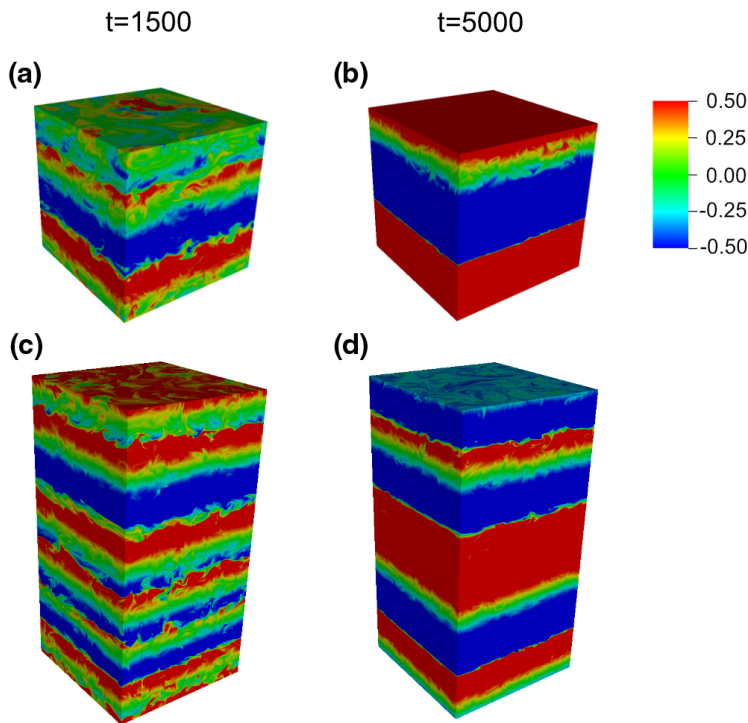


FIG. 3. Pseudocolor plots of the salinity field $S^{pr}(x, y, z, t)$ for simulation with $R_\rho = 5$ at time slices (a, c) $t = t_i = 1500$ and (b, d) $t = t_m = 5000$. (a, b) The normal box simulation (simulation 2) and (c, d) the tall box simulation (simulation 6).

the pseudocolor plot in Figs. 3(a) and 3(b), where we showed the salinity field at the initially formed staggered layered stage ($t = t_i = 1500$) and merged layered stage ($t = t_m = 5000$) for simulation 2. In order to test whether the layer formation process in the simulations is dependent upon the height of the domain, we compare the staircase state formed in simulation 2 (this will be referred to as the “normal box”) with that in simulation 6 that has twice the vertical domain height (this will be referred to as the “tall box”) while all other conditions remain the same. In the tall box simulation shown in Figs. 3(c) and 3(d), the staircases formed are somewhat unevenly distributed with step sizes varying at different vertical levels. There are five steps formed at time $t = 1500$ which later merged into three steps at $t = 5000$. This makes the averaged step sizes slightly lower but comparable with that of the normal box simulation at both these time slices. Furthermore, the turbulence characteristics also appear similar for the normal box domain and the tall box domain as can be seen in Fig. 3. Therefore we conclude that the time scale and the length scale of the staircase formation are not sensitive to the vertical domain height we have chosen. For this reason we will only discuss the normal box simulation of $R_\rho = 5$ in what follows to be consistent with other simulations. It is worth mentioning that although the three-step configuration shown in Fig. 3(d) is stable within our integration time of 6500 time units, we do not rule out the possibility that these staircases will eventually merge if this simulation is integrated much longer.

The important quantities for the layer formation and layer merging process are summarized in dimensional units in Table II. The unit transformation is made by relating the controlled nondimensional viscous dissipation rate with the typical value of viscous dissipation $\epsilon = 5 \times 10^{-9}$ W/kg (see [30], for example) in the Canada Basin. Using the typical value of molecular viscosity of $\nu = 1.8 \times 10^{-6}$ m²/s in the Arctic Ocean, we calculate the characteristic length scale for simulations 1–4 to be approximately $L_0 = 0.33$ m and the time scale to be approximately $L_0/U_0 = 60$ s.

TABLE II. Basic simulation results summarized for the five simulations performed. In this table, layering with “yes” or “no” indicates whether a layered structure observed to form in the system. t_i and t_m represent the time that the initially (staggered) layered state forms and the well-merged layered state is observed in the simulation, respectively. L is the step size in the finally merged layering state, and $h_{T\theta}$ and h_{T_s} are the interfacial thicknesses of the temperature profile and salinity profile in the equilibrium layered state.

No.	P	R_ρ	$\overline{\text{Re}}_b$	Layer	Steps	t_i (day)	t_m (day)	t_1 (day)	t_2 (day)	L (m)	$h_{T\theta}$ (m)	h_{T_s} (m)
1	0.01	2	9.5	Yes	4 \rightarrow 2	0.7	1.5	2.15	2.26	0.6	0.07	0.05
2	0.01	5	8.8	Yes	2 \rightarrow 1	0.9	3.6	5.05	5.27	1.3	0.11	0.08
3	0.01	8	8.8	Yes	2 \rightarrow 1	0.8	3.1	3.16	3.38	1.3	0.12	0.09
4	0.01	∞	8.7	Yes	2 \rightarrow 1	1.4	6.6	6.94	7.10	1.3	N.A.	0.10
5	0.1	2	83.0	No	N.A.	N.A.	N.A.	1.81	N.A.	N.A.	N.A.	N.A.

After transforming the characteristic times (t_i, t_m, t_1, t_2) to physical units as shown in Table II, we can see that it takes a time scale of several days for the layered structure to develop and merge into an equilibrated staircase. In our simulations, the step sizes L of these equilibrium staircase structures have a physical length scale of approximately 1 m. This is consistent with the measurements of the staircases in the Arctic Ocean, whose step sizes typically range from 1 to 5 m (e.g., [5]). This also shows that the choice of our vertical domain height in the numerical simulations is capable of capturing the real staircases formed in the Arctic Ocean. The interfacial thicknesses $h_{T\theta}$ and h_{T_s} formed in our simulations have been evaluated as the depth range within which $|\Theta_z| > 1$ and $|S_z| > 1$ are satisfied, respectively. The interfacial thicknesses have the order of 0.1 m, with the temperature interfaces generally thicker than the salinity interfaces due to the higher molecular diffusivity at the interface. These values match well with the interfacial thicknesses measured in the Canada Basin [51], where it was found that the temperature interfacial thicknesses are approximately 0.15 m. These consistencies in physical scales of the staircase structures suggest that the layered structures formed in our numerical simulations not only provide guidance for theoretical studies of the layer formation mechanism, but are also physically relevant for the actual staircases observed in the Arctic Ocean.

B. Comparison between the layer formation process in DNS analyses and theoretical predictions of thermohaline-turbulence instability

While we have shown that the thermohaline staircase structures do form naturally in our numerical system, in this section we will provide the analyses required to answer the question as to whether these layered structures form because of the thermohaline-turbulence instability discussed in MP21. In this process we will provide three tests on the basis of which to compare our numerical simulations with the predictions of thermohaline-turbulence instability theory in what follows. First, we will investigate whether the stability criterion derived from the theory is consistent with the layer formation process observed in our numerical simulations. Second, we will analyze whether or not the assumption of the parametrization scheme that lies at the heart of the thermohaline-turbulence instability [26] is operating in the current numerical system. Third, we will investigate whether the growth rate of the layering mode in our system is consistent with the growth rate predicted by the linear stability analysis. As we will demonstrate in what follows, the thermohaline-turbulence instability theory of MP21 provides rather good predictions for all these three aspects of the layer formation process.

We will start by evaluating the instability criterion of the thermohaline-turbulence instability. As we have reviewed in Sec. II, the thermohaline-turbulence instability theory predicts the layering instability of the system to occur only when the buoyancy Reynolds number satisfies the criterion $0.55 < \overline{\text{Re}}_b < 41$ [shown in Eq. (6)] for $\text{Pr} = 7$ and $\text{Sc} = 70$. In order to evaluate whether the instability criterion is satisfied, in Fig. 4 we show the evolution of $\overline{\text{Re}}_b$ in the five different

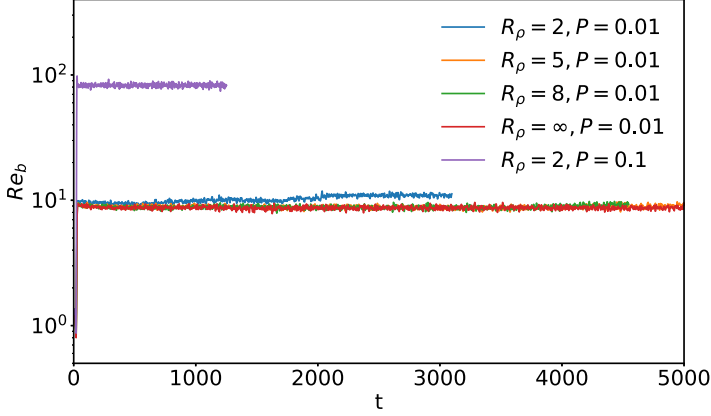


FIG. 4. Evolution of the volume-averaged buoyancy Reynolds number $\overline{\text{Re}}_b$ in simulations 1–5.

simulations we have performed. As expected, $\overline{\text{Re}}_b$ of the system self-adjusts to the level of approximately $\text{Re}P/J = 1000P$ [as discussed in Eq. (16)] soon after the introduction of the vortical modes forcing at $t = 20$. The fact that $\overline{\text{Re}}_b$ s of simulations 1–4 satisfy the criterion and $\overline{\text{Re}}_b$ of simulation 5 exceeds the criterion is consistent with our observations described in the last section that the layered structure forms in simulations 1–4 but not in simulation 5. Another interesting thing to notice in Fig. 4 is that the level of $\overline{\text{Re}}_b$ is slightly higher for $R_\rho = 2$ than for the other simulations with $P = 0.01$. This is a consequence of the buoyancy flux becoming negative in this case (shown previously in Fig. 2) which provides an additional net energy source to be dissipated. The time-averaged value of $\overline{\text{Re}}_b$ for the layer growing stage of each simulation is averaged over time periods of $t = 50$ to $t = t_i$ to be shown in Table II.

Next we turn to evaluate the effectiveness of the parametrization scheme described in Eq. (7) in the current numerical system. To do this we need to compute the diapycnal diffusivities K_Θ and K_S at different vertical depths of our system and evaluate whether they are strongly correlated with the local buoyancy Reynolds number Re_b . To reduce the influence of advection that varies strongly with time, we evaluate the time-averaged one-dimensional buoyancy Reynolds number $\overline{\text{Re}}_b(z)$ and diapycnal diffusivities $\widetilde{K}_\Theta(z)$ and $\widetilde{K}_S(z)$ following

$$\begin{aligned}
 \widetilde{\Theta}_z(z) &\equiv \left\langle \frac{\partial \overline{\Theta}(z, t)}{\partial z} \right\rangle_t, & \widetilde{S}_z(z) &\equiv \left\langle \frac{\partial \overline{S}(z, t)}{\partial z} \right\rangle_t, & \widetilde{N}^2(z) &\equiv -\frac{1}{J} \left(\frac{R_\rho}{R_\rho - 1} \widetilde{S}_z - \frac{1}{R_\rho - 1} \widetilde{\Theta}_z \right), \\
 \widetilde{\epsilon}(z) &\equiv \langle \overline{2s_{ij}s_{ij}}(z, t) \rangle_t, & \widetilde{\text{Re}}_b(z) &\equiv \frac{\widetilde{\epsilon}(z)}{N^2(z)}, & \widetilde{F}_\Theta(z) &\equiv \langle \overline{w'\Theta'}(z, t) \rangle_t - \frac{1}{\text{RePr}} \widetilde{\Theta}_z(z), \\
 \widetilde{F}_S(z) &\equiv \langle \overline{w'S'}(z, t) \rangle_t - \frac{1}{\text{ReSc}} \widetilde{S}_z(z), & \widetilde{K}_\Theta(z) &\equiv -\frac{\widetilde{F}_\Theta(z)}{\widetilde{\Theta}_z(z)}, & \widetilde{K}_S(z) &\equiv -\frac{\widetilde{F}_S(z)}{\widetilde{S}_z(z)}.
 \end{aligned} \tag{19}$$

In the above equations and throughout the rest of the paper, $\langle \cdot \rangle_t$ represents the time averages over the chosen time intervals and the tilde symbol over a physical quantity represents that it is averaged in (x, y, t) but not in z . \widetilde{F}_Θ and \widetilde{F}_S represent time-averaged vertical heat and salt fluxes which include the contribution from both the convective fluxes and the diffusive fluxes.

In order to focus on the layer formation stage of the evolution, we evaluated $\widetilde{K}_\Theta(z)$, $\widetilde{K}_S(z)$, and $\widetilde{\text{Re}}_b(z)$ over 40 nondimensional units of time intervals centered at $t = 0.5t_i$ for simulations 1–4 and at $t = t_i - 20$ for simulation 5. These depth-dependent data are further averaged into 50 small depth intervals for the correlation study. In Figs. 5(a) and 5(b), we plot the depth variations of dissipation ratio $\widetilde{\epsilon}(z)$ and $\widetilde{\text{Re}}_b(z)$ defined in Eqs. (19) above. By comparing these two figures, we conclude that the variations of $\widetilde{\text{Re}}_b(z) = \widetilde{\epsilon}/N^2$ are mainly contributed from $N^2(z)$ instead of $\widetilde{\epsilon}(z)$ since $\widetilde{\epsilon}(z)$ shows

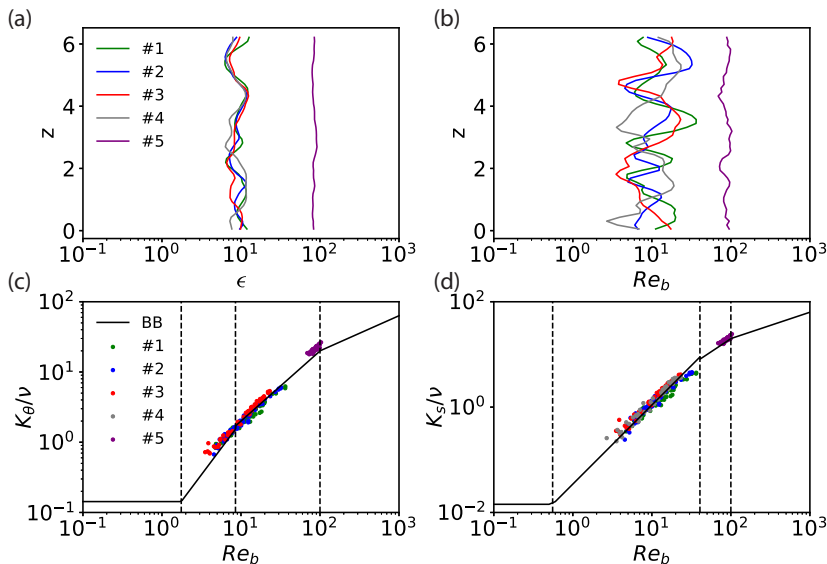


FIG. 5. Depth dependence of (a) $\tilde{\epsilon}$ and (b) \tilde{Re}_b . Scatter plot of (c) $(\tilde{Re}_b, \tilde{K}_\Theta)$ and (d) $(\tilde{Re}_b, \tilde{K}_S)$ in (Re_b, K) parameter space at different vertical coordinates. The black solid line shows the parametrization scheme of Eqs. (7) for (c) temperature and (d) salinity. The vertical dashed lines represent the critical Re_b values that separate different parametrization regions in Eqs. (7). All physical quantities are evaluated at the time interval $(0.5t_i - 20, 0.5t_i + 20)$ for simulations 1–4 and at $(t_1 - 40, t_1)$ for simulation 5.

very small vertical variations. This fact suggests that the assumption we made in the derivation of Eq. (3) described in Sec. II, namely, the viscous dissipation is a constant and only $N^2(z)$ feeds back on $Re_b(z)$, is a fair assumption in describing the current numerical system. In Figs. 5(c) and 5(d) we further plot $\tilde{K}_\Theta(z)$, $\tilde{K}_S(z)$, and $\tilde{Re}_b(z)$ in the (Re_b, K) parameter space to be compared with the parametrization [26] evaluated from Eqs. (7). It can be clearly seen in this figure that the distribution of $\tilde{Re}_b(z)$ at different depths spans approximately an order of magnitude due to the growth of perturbations in the system [also shown in Fig. 5(b)]. In such a wide range of $\tilde{Re}_b(z)$ the diapycnal diffusivities $\tilde{K}_\Theta(z)$ and $\tilde{K}_S(z)$ follow the predictions of [26] very well, except for slight deviations of K_Θ in the small Re_b regions. Most importantly the key element of the parametrization from [26] needed to support the thermohaline-turbulence instability theory, namely, the existence of the buoyancy-controlled regime for K_S that scales as $Re_b^{3/2}$, is well captured in the current system as shown in Fig. 5(d). This strongly implies that the theoretical derivations in MP21 are based on reasonable assumptions which are confirmed in our current numerical system.

Finally, we will perform a detailed analysis of the vertical wavenumber spectrum for temperature and salinity to compare the theoretical predictions of MP21 with the growth rate of the layering mode of instability. Specifically, we perform the vertical Fourier transformation of the horizontally averaged salinity field (or temperature field) following

$$\begin{aligned}
 S_m(t) &= \frac{1}{V} \int_V S(x, y, z, t) e^{imz} dV, \\
 \Theta_m(t) &= \frac{1}{V} \int_V \Theta(x, y, z, t) e^{imz} dV,
 \end{aligned} \tag{20}$$

where m must take integer values as constrained by our triplet periodic domain with size 2π . In Figs. 6(a)–6(d) we show the evolution of the vertical wavenumber spectrum of salinity S_m (temperature spectrum looks similar) for simulations 1–4. The evolution of the spectrum confirms

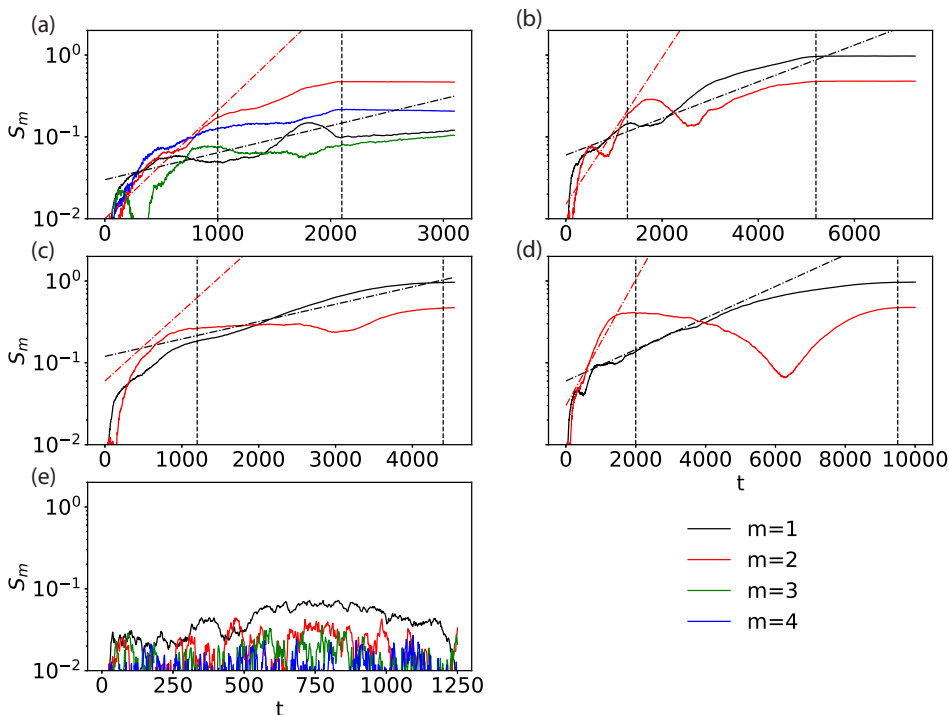


FIG. 6. Evolution of the vertical spectrum of salinity for various modes S_m as a function of time in simulations 1–5. The dash-dotted line [in (a)–(d)] represents the growth rate λ for each mode predicted from the linear stability analysis calculated from formulas (4). The vertical dashed line [in (a)–(d)] marks the characteristic time t_i and t_m sequentially.

our observations described in the last section concerning the different stages of the evolution: for simulation with $R_\rho = 2$ shown in Fig. 6(a), the system is first dominated by the $m = 4$ mode until the growth of the $m = 2$ mode finally dominates the system and stays steady. We can also see the formation of the two-layer state for $R_\rho = 5$, $R_\rho = 8$, and $R_\rho = \infty$ before the final formed single-layer staircase in Figs. 6(b)–6(d). For comparison simulation 5, however, there is no sign of layer formation in Fig. 6(e).

The evolution of the vertical wavenumber spectrum can be compared with the growth rate predicted by the theory described in Sec. II. The linear growth rates are calculated based on Eq. (4) using $\overline{\text{Re}_b}$ and R_ρ for each simulation and they are represented as the dash-dotted lines in Figs. 6(a)–6(d). It can be seen from the figure that the thermohaline-turbulence instability theory offers a fairly good prediction for the growth of the first two vertical modes $m = 1$ and $m = 2$ before saturation. This fact further supports the effectiveness of the theory of MP21.

To summarize the results of this section, we have demonstrated the effectiveness of the thermohaline-turbulence instability theory from three perspectives. First, we showed that the instability criterion provided correct predictions of whether the layers would form in the system. Second, we justified the key assumption made in the theory, namely, the parametrization scheme of [26] provides an accurate description of our system. Finally we have demonstrated that the growth of the governing layering mode is consistent with the prediction of the linear stability analysis. Therefore, we conclude that the spontaneous formation of the layered structure in our system is indeed triggered by the thermohaline-turbulence instability theory described by MP21.

It should also be clear on the basis of the previous discussions that while Re_b solely determines whether the layered structure will form in the DNS system, it seems that R_ρ plays a role in

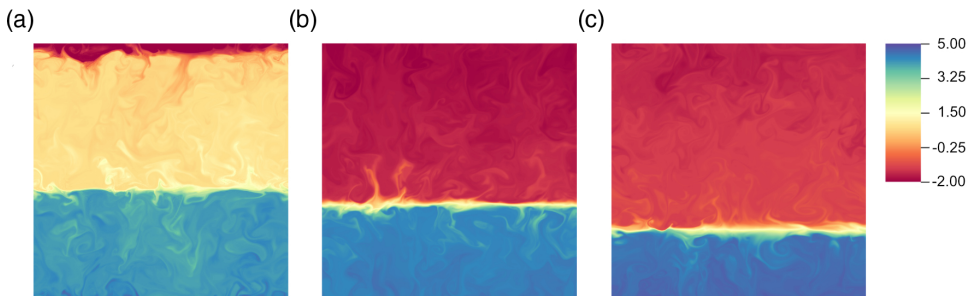


FIG. 7. Density fields for the equilibrium staircases at $t = t_2$ for simulation with (a) $R_\rho = 2$, (b) $R_\rho = 5$, and (c) $R_\rho = 8$. The pseudocolor plot is performed for the x - z plane at the y midpoint of the three-dimensional domain.

determining the step size of the initially formed layering mode, considering that the number of layers formed in our simulations varies with R_ρ . The explanation of the depth of the first formed layers in the system is not predictable on the basis of MP21 and goes beyond the scope of the present paper. In order to fully understand this problem, we need a multiscale model that captures the response of gradients at smaller scales, an example of which is provided in the work of [16] that focused upon the salt-fingering regime of double-diffusive convection.

V. DIFFUSIVE CONVECTION STAIRCASE STRUCTURE IN THE DIRECT NUMERICAL SIMULATIONS

As we have demonstrated above, the thermohaline staircase structures form spontaneously in our continuously forced system. A natural and critical further objective of the present work is to analyze the detailed steady structure of the formed diffusive convection staircases. In order to achieve this, we have integrated the staircase state of the system ($t = t_1$) with the doubled resolution for an additional short period until the system reaches its steady state with this high resolution at $t = t_2$ (the values of t_2 have been summarized in Table II). The better resolved domain allows us to look closely at the morphology and the vertical transport, which will be discussed in Sec. V A. In Sec. V B, we will compare our simulated interfaces with the existing theory of diffusive interfaces proposed by LS.

A. Staircase structure

In Fig. 7, we show the vertical cross sections of the density field at the equilibrium state of the high-resolution run for simulations with $R_\rho = 2, 5$, and 8. As discussed previously, while the two-step layered state forms with $R_\rho = 2$ at the end of our numerical simulation, simulations with $R_\rho = 5$ and $R_\rho = 8$ have the single-layer structure across the vertical domain. In all these simulations, very sharp interface(s) can be observed to separate well-mixed convective layers below and above. Thin plumes can be observed in these fields to rise from the interfaces to transport scalars into the mixed layers. These plumes have also been observed in the previous numerical simulations of diffusive interfaces (e.g., [32,52]) and they have been argued as the crucial structure in transporting scalars from the interface into the mixed layers [53].

In order to facilitate a further quantitative analysis of the layered structure, in Fig. 8 we show the vertical distribution of heat and salt fluxes ($\widetilde{F}_\Theta(z), \widetilde{F}_S(z)$), vertical gradients of temperature and salinity ($\widetilde{\Theta}_z(z), \widetilde{S}_z(z)$), as well as the effective vertical diffusivities for temperature and salinity ($\widetilde{K}_\Theta(z), \widetilde{K}_S(z)$) of the system, all evaluated at the nondimensional time interval of $(t_2 - 40, t_2)$ in the steady state of the high-resolution run for our simulations with $R_\rho = 2, 5$, and 8. As shown in Figs. 8(c), 8(f), and 8(i), the vertical diffusivities are significantly different in the mixed layers

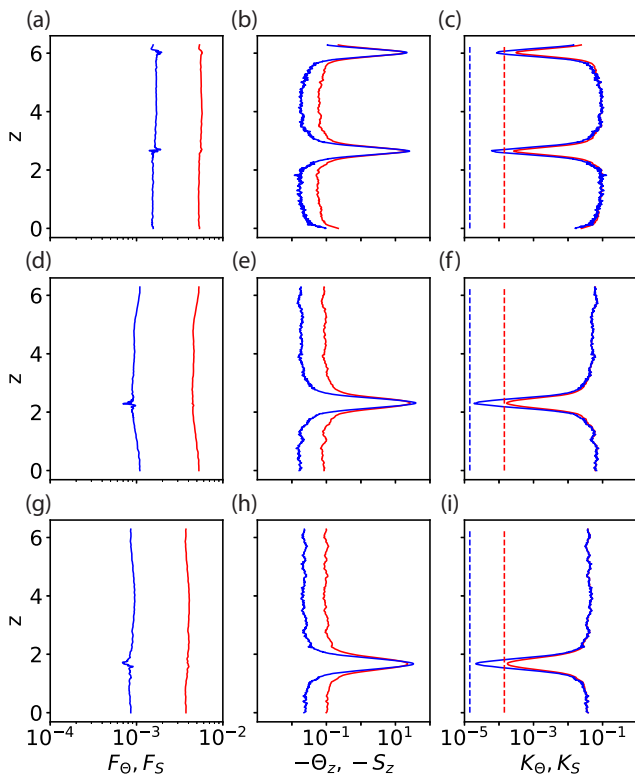


FIG. 8. Time-averaged vertical fluxes for heat and salt, $\widetilde{F}_\Theta(z)$ and $\widetilde{F}_S(z)$, vertical gradients for temperature and salinity, $\widetilde{\Theta}_z(z)$ and $\widetilde{S}_z(z)$, and diapycnal diffusivities for heat and salt, $\widetilde{K}_\Theta(z)$ and $\widetilde{K}_S(z)$, evaluated at the nondimensional time interval $(t_2 - 40, t_2)$ for simulation with (a–c) $R_\rho = 2$, (d–f) $R_\rho = 5$, and (g–i) $R_\rho = 8$. In this figure, we use red to represent the temperature-related physical quantities and blue to represent the salinity-related physical quantities.

compared with the interface regions, suggesting entirely different dynamics in those regions: in the mixed layers, mixing is driven by strong turbulent convection which leads to the same values of diffusivities for heat and salt. In the interface region(s), however, the turbulent diffusivities for heat and salt are the same order as the molecular diffusivities for temperature and salinity, suggesting the absence of turbulent motions at the interface region. Furthermore, the turbulent diffusivities at the interfaces are lower for $R_\rho = 5$ and 8 compared with $R_\rho = 2$. This is possibly because the scalar variations across the interfaces are higher for $R_\rho = 5$ and 8 compared with $R_\rho = 2$ (as shown in Fig. 7), which makes it more difficult for the turbulence in the mixed layers to penetrate the interfaces.

Even though the vertical diffusivities in the mixed layer regions are two to three orders of magnitude higher than in the interface regions, the vertical scalar gradients in the mixed layers are two to three orders of magnitude lower than in the interface regions [shown in Figs. 8(b), 8(e), and 8(h)], which leads to the crude balance of vertical fluxes shown in Figs. 8(a), 8(d), and 8(g). The maintenance of flux balances between the mixed layers and interface regions suggested that the staircase structures formed in our system can stably persist.

B. Comparison with the classical diffusive-interface model

While we have illustrated how the steady staircase structure is maintained by the balance of heat and salt flux between interface regions and mixed layers, we will compare these structures with the

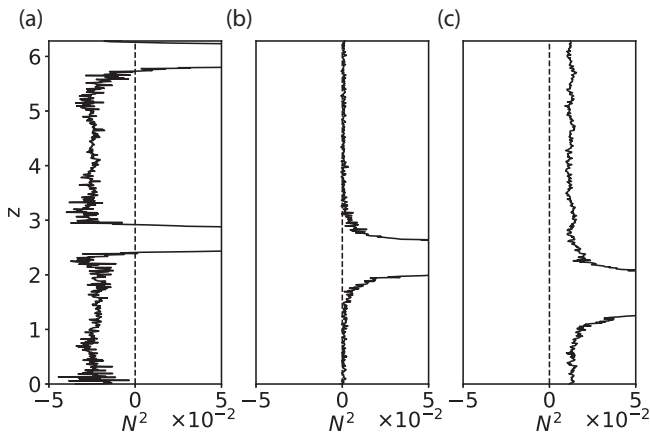


FIG. 9. Time-averaged buoyancy frequency \widetilde{N}^2 in the mixed layers as a function of depth evaluated at the nondimensional time interval $(t_2 - 40, t_2)$ for simulations with (a) $R_\rho = 2$, (b) $R_\rho = 5$, and (c) $R_\rho = 8$.

classical theoretical model of diffusive interfaces of LS. LS presented a time-independent model of diffusive interfaces, which provides significant insights concerning the following theoretical and numerical simulations of diffusive interfaces studies (see review of [34,50]). In this model, the interface consists of two boundary layers from which fluctuations arise on the outer edge of the interfaces and a diffusive core cross in which transport takes place only by molecular diffusion. This theoretical model describes a diffusive-interface structure that can only remain stable when the density ratio R_ρ is smaller than the critical value of $R_\rho^{cr} = \tau^{-1/2}$. The LS model was later extended in [54,55] to include the run-down evolution of the diffusive interfaces in the $R_\rho > R_\rho^{cr}$ regime. As the diffusive interface structure is spontaneously formed and kept stable in our numerical simulations, the run-down model of [54,55] will be irrelevant to our current discussions. Therefore we will focus on comparing our interface structures only with the original time-independent model of LS.

In our system, $R_\rho^{cr} = \tau^{-1/2} = 3.16$ so that the small R_ρ simulation $R_\rho = 2$ satisfies the criterion while the large R_ρ simulations with $R_\rho = 5$ and 8 are outside of the criterion. To investigate whether the unstably stratified boundary layers described in the LS theory are formed in these simulations, we plot in Fig. 9 the time-averaged and horizontally averaged buoyancy frequency \widetilde{N}^2 defined in Eq. (19) for $R_\rho = 2, 5$, and 8 . As shown in Figs. 9(b) and 9(c), the unstably stratified boundary layers, which are characterized by the $N^2 < 0$ region above and below the interface, do not exist for the large R_ρ staircases $R_\rho = 5$ and $R_\rho = 8$. For $R_\rho = 2$, on the other hand, N^2 takes negative values in a wide range of depth regions. While this fact shows that the boundary layer structure is not special in keeping the staircases stable in our model, it does not contradict the LS theory considering that the water columns do become unstably stratified below and above the interface core.

In order to further test whether our $R_\rho = 2$ simulation is consistent with LS's model, in Fig. 10 we plot the time-averaged density ratio $\widetilde{R}_\rho(z) \equiv \widetilde{S}_z / \widetilde{\Theta}_z$ and $\widetilde{\gamma}(z) \equiv \widetilde{F}_S / \widetilde{F}_\Theta$ in the steady state of our system. LS's original theory predicted that the value of \widetilde{R}_ρ and $\widetilde{\gamma}$ at the interface will be determined by $1/\sqrt{\tau}$ and $\sqrt{\tau}$, respectively. As later pointed out in [56] and developed in the recent work of [33], the molecular diffusivity ratio τ in LS's original theory should be replaced by the ratio of effective diffusivity $\tau^{\text{eff}} = K_S / K_\Theta$ across the interface when the interface is influenced by turbulence. The predicted values from this slightly revised theory are evaluated and plotted as the vertical dash-dotted line in Fig. 10. From this figure it can be observed that the predicted values of interface R_ρ and interface γ are approximately 10% and 20% lower than the simulated values, respectively.

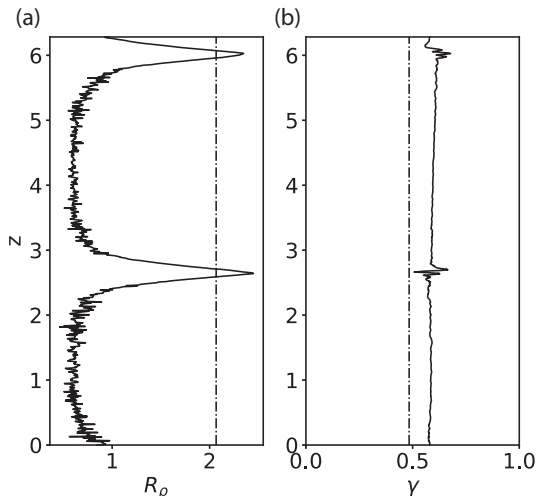


FIG. 10. (a) Time-averaged density ratio $\tilde{R}_\rho(z)$ and (b) flux ratio $\tilde{\gamma}(z)$ (solid lines) evaluated at the nondimensional time interval $(t_2 - 40, t_2)$ for simulation 1 ($R_\rho = 2$), in comparison with the predicted value of from LS's theory (vertical dash-dotted lines).

As discussed above, while our small R_ρ simulation with $R_\rho = 2$ is still more or less consistent with LS's model, our simulations with $R_\rho = 5$ and $R_\rho = 8$ cannot be explained by LS's model. In order to understand this inconsistency, two important distinctions between our numerical model and the original theoretical model of LS should be recognized: First, the theoretical model of LS assumed perfectly homogenized mixed layers above and below the interfaces. As shown in Figs. 8(b), 8(e), and 8(h), however, a fully equilibrated staircase structure requires finite values (although small) of vertical gradients for both temperature and salinity in the mixed layers. In this circumstance, as discussed above, the balance between vertical fluxes in the mixed layers and those in the interfaces is the key to maintaining the staircase structure. This clearly goes beyond the description of the simplified LS model which only discussed the interface transportation. Second, the theoretical model of LS is a purely buoyancy-driven model which does not include any effect of dynamically driven stratified turbulence. Without stratified turbulence, the unstably stratified boundary layer becomes necessary for their model to transport the diffusive fluxes at the sharp interfaces into the mixed layers. However, when the effect of stratified turbulence is properly taken into account in our model, the flux balance between interface and mixed layers can be established (see Fig. 8) without the presence of any unstably stratified boundary layer. Therefore the staircase structure can stably exist in our systems with $R_\rho > R_\rho^{cr}$ even though they are predicted to be unstable by LS's theory.

VI. SUMMARY AND CONCLUSIONS

In this paper, we have performed a series of DNS analyses of the continuously forced stratified turbulence system comprised of two different scalars stratified in the diffusive-convection configuration. We found that the thermohaline layered structure forms spontaneously in the simulations. We then considered three different aspects of this process to show that it is indeed well explained by the theory of thermohaline-turbulence instability proposed by MP21. First, we showed that the controlled parameter \overline{Re}_b in the layering simulations does satisfy the criterion derived by MP21. Second, we have demonstrated that the key assumption of the thermohaline-turbulence instability theory of MP21, namely, that the parametrization scheme [26] determines the vertical transports of the system, is indeed the case in the layer formation stage of the evolution of our system.

Third, we have found good consistency between the exponential growth of the layering mode and the predicted growth rate from the linear theory of MP21. These results strongly suggest that the thermohaline-turbulence instability theory is the highly plausible explanation of thermohaline staircase formation in the diffusive convection regime, for example, in the Arctic Ocean.

The staircases formed in our DNSs were next examined and compared with the model proposed by LS. We explained how the vertical fluxes are kept balanced vertically in our model despite the fact that the boundary layer structure, which has been regarded as critical in stabilizing the interface structure, is missing in our model. We have argued that the reason for the discrepancies between the classic model and our simulations is that the effect of stratified turbulence at the boundary layers and mixed layers has not been considered in this classic model.

There are several limitations of the numerical simulations discussed in this paper. First, we have assumed a Schmidt number $Sc = 70$ in our simulations which is at least an order of magnitude smaller than the actual Schmidt number in the ocean. This prevents us from directly comparing the values of fluxes obtained from our simulations with the empirical interface flux laws calibrated previously (e.g., [53,57,58]). Second, we do not yet know whether the steady staircase state we observed is in its final equilibrium state. It is possible that after a much longer integration time (and higher domains) the current stable stabilized staircases will continue to merge. Observing such trends in DNSs requires a considerable number of computational resources.

From the theoretical perspective, the current thermohaline-turbulence instability is still based on the mean-field equation (1) which suffers from the ultraviolet catastrophe (same caveats as [8]) in the small-scale limits. This fact restricts our ability to predict the step sizes that initially form in our system (as we have mentioned previously at the end of Sec. IV B). It also prevents us from applying the parametrization from [26] directly to the thin diffusive interface structure to infer its vertical fluxes. Therefore, we believe that a properly captured multiscale theory as has been done in the salt-fingering staircase [16] is the key to a deeper understanding of the diffusive-convection staircases.

ACKNOWLEDGMENTS

The authors sincerely thank two anonymous referees for helping us to improve the article. Financial support under the NSERC Discovery Grant No. A9627 is gratefully acknowledged. The computations on which this paper is based were performed on the Niagara cluster at the SciNet High Performance Computing facility at the University of Toronto funded by the Canadian Foundation for Innovation, the Province of Ontario and the University of Toronto.

APPENDIX: INFLUENCES OF RESOLUTION ON THE DIRECT NUMERICAL SIMULATIONS

As discussed in the main text, the long integration time needed for the system to develop into the staircase state exerts a strong constraint on the resolution available for our numerical simulations. In order to understand the influences of resolution in our numerical system, we performed three control experiments for simulations 1–3 with the same numerical settings except for a coarser resolution with half the number of grid points in each of three spatial dimensions ($175 \times 175 \times 175$ grid points). In what follows, we will use “low-res,” “mid-res,” and “high-res” to refer to the resolutions of $175 \times 175 \times 175$, $350 \times 350 \times 350$, and $700 \times 700 \times 700$ grids, respectively.

In Figures 11(a)–11(c) we compare the evolution of the vertical spectrum of salinity for the critical layering mode between “low-res” simulation and “mid-res” simulation (spectrum evolution of “mid-res” has been shown and discussed in the main text) for $R_\rho = 2, 5, \text{ and } 8$ with $P = 0.01$. Although the systems take a different path and different periods towards the equilibrium as we switched the resolution, the equilibrium states for the vertical structure they reach are almost identical. This can be seen in Figs. 11(d)–11(f), which show the comparison of vertical profiles for temperature and salinity between “low-res” simulations and “mid-res” simulations in the equilibrium state. These vertical profiles show almost the same structure except for the fact that

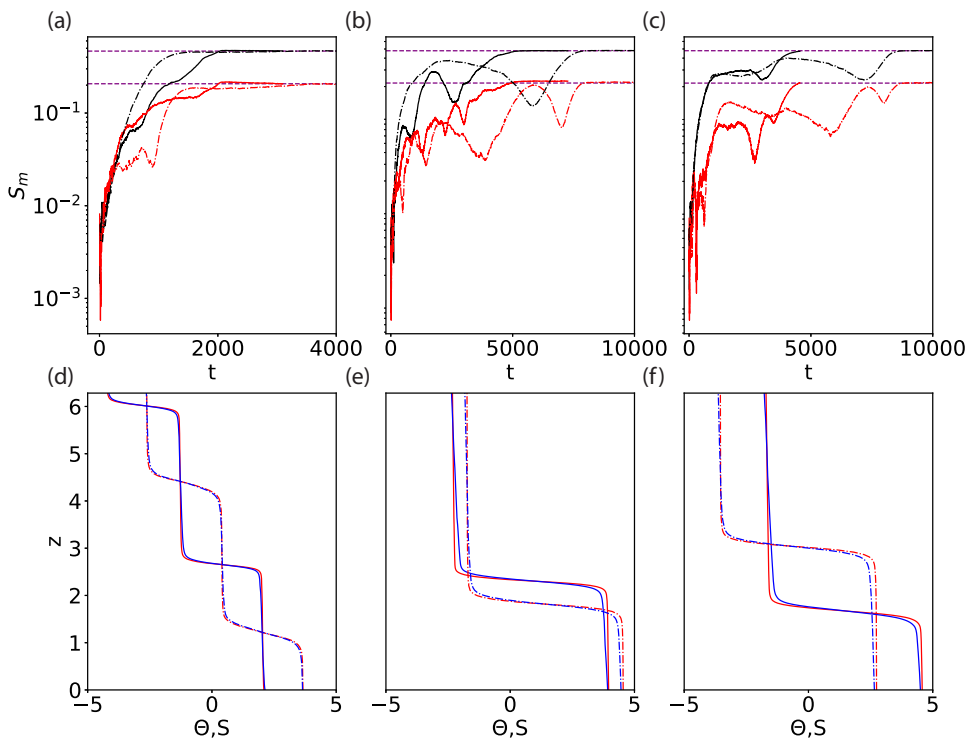


FIG. 11. (a–c) Comparison of vertical spectrum of salinity between “low-res” simulation (dash-dotted lines) and “mid-res” simulation (solid lines) for (a) $R_\rho = 2$, (b) $R_\rho = 5$, and (c) $R_\rho = 8$. For $R_\rho = 2$ we use black to represent the $m = 2$ mode and red to represent the $m = 4$ mode. For $R_\rho = 5$ and $R_\rho = 8$ we use black to represent the $m = 1$ mode and red to represent the $m = 2$ mode. (d–f) Comparison of vertical profiles of $\bar{\Theta}(z)$ and $\bar{S}(z)$ in the equilibrium staircase state between “low-res” simulation (dash-dotted lines) and “mid-res” simulation (solid lines). The temperature profile is shown in red and the salinity profile is shown in blue.

the interface gradients for low-res simulation are slightly smaller for $R_\rho = 2$. This suggests that the formation of the staircase state in our numerical system is a robust result instead of a numerical artifact.

Although the variation of resolution does not influence the final equilibrium staircase state of our numerical simulations, the vertical heat flux and salt flux in the equilibrium state are found to be sensitive to the resolutions. To see this, we evaluate the Nusselt numbers for heat and salt, which are the commonly used nondimensional numbers that reflect the ratio of convective flux over diffusive flux defined as

$$\text{Nu}_\Theta = \text{RePr}\langle w'\Theta'\rangle, \quad \text{Nu}_S = \text{ReSc}\langle w'S'\rangle. \quad (\text{A1})$$

In Fig. 12, we plot the variation of the Nusselt numbers as a function of three different resolutions applied in the equilibrium layered stage in our simulations with $R_\rho = 2, 5$, and 8, respectively. Both Nu_Θ and Nu_S vary with the increased resolution for all our simulations, especially for the strong increase of Nu_S from low-res simulation to mid-res simulation. The fact that only mild variations of fluxes occur during the improvement of resolution from “mid-res” to “high-res” suggests that further increase of resolution will not bring significant variation to the equilibrium transport we have simulated. However, it still needs to be remembered that these values of fluxes we have obtained are under limited resolution and should be viewed cautiously.

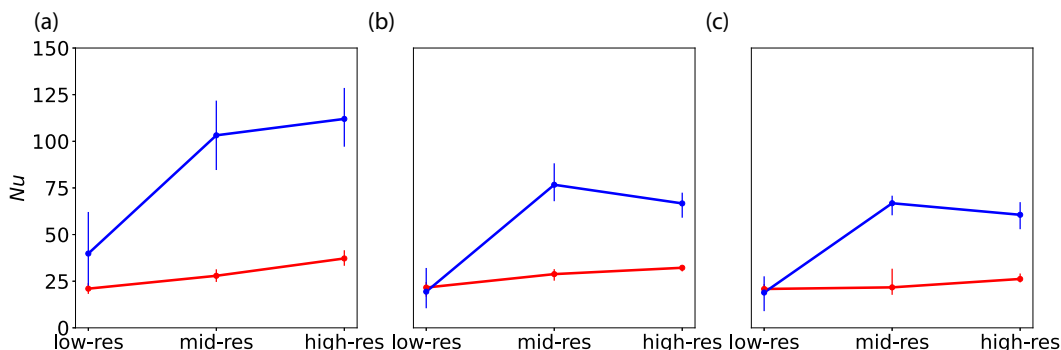


FIG. 12. (a–c) Comparison of Nusselt numbers Nu_Θ (red) and Nu_S (blue) in the equilibrium layered stage at different resolutions for simulations with (a) $R_\rho = 2$, (b) $R_\rho = 5$, and (c) $R_\rho = 8$. The lower and upper error bars are calculated based on the 5% quantile and the 95% quantile of the Nu data, respectively.

- [1] T. Radko, *Double-Diffusive Convection* (Cambridge University Press, Cambridge, UK, 2013).
- [2] R. W. Schmitt, J. Ledwell, E. Montgomery, K. Polzin, and J. Toole, Enhanced diapycnal mixing by salt fingers in the thermocline of the tropical Atlantic, *Science* **308**, 685 (2005).
- [3] G. Zodiatis and G. P. Gasparini, Thermohaline staircase formations in the Tyrrhenian Sea, *Deep Sea Res. Part I* **43**, 655 (1996).
- [4] R. Muench, H. J. Fernando, and G. Stegen, Temperature and salinity staircases in the northwestern Weddell Sea, *J. Phys. Oceanogr.* **20**, 295 (1990).
- [5] M.-L. Timmermans, J. Toole, R. Krishfield, and P. Winsor, Ice-tethered profiler observations of the double-diffusive staircase in the Canada Basin thermocline, *J. Geophys. Res. Oceans* **113**, C00A02 (2008).
- [6] R. Tait and M. Howe, Some observations of thermo-haline stratification in the deep ocean, in *Deep Sea Research and Oceanographic Abstracts*, Vol. 15 (Elsevier, Amsterdam, 1968), pp. 275–280
- [7] V. T. Neal, S. Neshyba, and W. Denner, Thermal stratification in the Arctic Ocean, *Science* **166**, 373 (1969).
- [8] T. Radko, A mechanism for layer formation in a double-diffusive fluid, *J. Fluid Mech.* **497**, 365 (2003).
- [9] M. E. Stern, T. Radko, and J. Simeonov, Salt fingers in an unbounded thermocline, *J. Mar. Res.* **59**, 355 (2001).
- [10] A. Traxler, S. Stellmach, P. Garaud, T. Radko, and N. Brummell, Dynamics of fingering convection. Part 1: Small-scale fluxes and large-scale instabilities, *J. Fluid Mech.* **677**, 530 (2011).
- [11] T. Radko and D. P. Smith, Equilibrium transport in double-diffusive convection, *J. Fluid Mech.* **692**, 5 (2012).
- [12] Y. Ma and W. Peltier, Parametrization of irreversible diapycnal diffusivity in salt-fingering turbulence using DNS, *J. Fluid Mech.* **911**, A9 (2021).
- [13] S. Stellmach, A. Traxler, P. Garaud, N. Brummell, and T. Radko, Dynamics of fingering convection. Part 2: The formation of thermohaline staircases, *J. Fluid Mech.* **677**, 554 (2011).
- [14] T. Radko, A. Bulters, J. Flanagan, and J.-M. Campin, Double-diffusive recipes. Part I: Large-scale dynamics of thermohaline staircases, *J. Phys. Oceanogr.* **44**, 1269 (2014).
- [15] T. Radko, What determines the thickness of layers in a thermohaline staircase? *J. Fluid Mech.* **523**, 79 (1999).
- [16] T. Radko, Thermohaline layering on the microscale, *J. Fluid Mech.* **862**, 672 (2019).
- [17] Y. Ma and W. R. Peltier, Gamma instability in an inhomogeneous environment and salt-fingering staircase trapping: Determining the step size, *Phys. Rev. Fluids* **6**, 033903 (2021).
- [18] R. W. Schmitt, Double diffusion in oceanography, *Annu. Rev. Fluid Mech.* **26**, 255 (1994).
- [19] N. Shibley, M.-L. Timmermans, J. Carpenter, and J. Toole, Spatial variability of the Arctic Ocean’s double-diffusive staircase, *J. Geophys. Res. Oceans* **122**, 980 (2017).

- [20] T. Radko, Thermohaline layering in dynamically and diffusively stable shear flows, *J. Fluid Mech.* **805**, 147 (2016).
- [21] J. M. Brown and T. Radko, Initiation of diffusive layering by time-dependent shear, *J. Fluid Mech.* **858**, 588 (2019).
- [22] T. Radko, Thermohaline-shear instability, *Geophys. Res. Lett.* **46**, 822 (2019).
- [23] W. J. Merryfield, Origin of thermohaline staircases, *J. Phys. Oceanogr.* **30**, 1046 (2000).
- [24] Y. Bebieva and M.-L. Timmermans, The relationship between double-diffusive intrusions and staircases in the Arctic Ocean, *J. Phys. Oceanogr.* **47**, 867 (2017).
- [25] Y. Ma and W. Peltier, Thermohaline staircase formation in the diffusive convection regime: A theory based upon stratified turbulence asymptotics, *J. Fluid Mech.* **931**, R4 (2022).
- [26] D. Bouffard and L. Boegman, A diapycnal diffusivity model for stratified environmental flows, *Dyn. Atmos. Ocean* **61-62**, 14 (2013).
- [27] O. Phillips, Turbulence in a strongly stratified fluid—is it unstable?, in *Deep Sea Research and Oceanographic Abstracts*, Vol. 19 (Elsevier, Amsterdam, 1972), pp. 79–81.
- [28] J. Taylor and Q. Zhou, A multi-parameter criterion for layer formation in a stratified shear flow using sorted buoyancy coordinates, *J. Fluid Mech.* **823**, R5 (2017).
- [29] Y. Ma and W. Peltier, Diapycnal diffusivities in Kelvin Helmholtz engendered turbulent mixing: The diffusive convection regime in the Arctic Ocean, *J. Fluid Mech.* (2022), doi:10.1017/jfm.2022.590.
- [30] H. Dosser, M. Chanona, S. Waterman, N. Shibley, and M.-L. Timmermans, Changes in internal wave-driven mixing across the Arctic Ocean: Finescale estimates from an 18-year pan-Arctic record, *Geophys. Res. Lett.* **48**, e2020GL091747 (2021).
- [31] P. Linden and T. Shirtcliffe, The diffusive interface in double-diffusive convection, *J. Fluid Mech.* **87**, 417 (1978).
- [32] J. Carpenter, T. Sommer, and A. Wüest, Simulations of a double-diffusive interface in the diffusive convection regime, *J. Fluid Mech.* **711**, 411 (2012).
- [33] N. Shibley and M.-L. Timmermans, The formation of double-diffusive layers in a weakly turbulent environment, *J. Geophys. Res. Oceans* **124**, 1445 (2019).
- [34] D. Kelley, H. Fernando, A. Gargett, J. Tanny, and E. Özsoy, The diffusive regime of double-diffusive convection, *Prog. Oceanogr.* **56**, 461 (2003).
- [35] J. Turner, A physical interpretation of the observations of hot brine layers in the Red Sea, in *Hot Brines and Recent Heavy Metal Deposits in the Red Sea* (Springer, Berlin, 1969), pp. 164–173.
- [36] A. Boldrin and S. Rabitti, Hydrography of the brines in the Bannock and Tyro anoxic basins (eastern Mediterranean), *Mar. Chem.* **31**, 21 (1990).
- [37] M. L. Waite and P. Bartello, Stratified turbulence dominated by vortical motion, *J. Fluid Mech.* **517**, 281 (1999).
- [38] G. Brethouwer, P. Billant, E. Lindborg, and J.-M. Chomaz, Scaling analysis and simulation of strongly stratified turbulent flows, *J. Fluid Mech.* **585**, 343 (2007).
- [39] A. Maffioli, G. Brethouwer, and E. Lindborg, Mixing efficiency in stratified turbulence, *J. Fluid Mech.* **794**, R3 (2016).
- [40] C. J. Howland, J. R. Taylor, and C. Caulfield, Mixing in forced stratified turbulence and its dependence on large-scale forcing, *J. Fluid Mech.* **898**, A7 (2020).
- [41] L. H. Shih, J. R. Koseff, G. N. Ivey, and J. H. Ferziger, Parameterization of turbulent fluxes and scales using homogeneous sheared stably stratified turbulence simulations, *J. Fluid Mech.* **525**, 193 (2005).
- [42] H. Salehipour, W. Peltier, C. Whalen, and J. MacKinnon, A new characterization of the turbulent diapycnal diffusivities of mass and momentum in the ocean, *Geophys. Res. Lett.* **43**, 3370 (2016).
- [43] W. Smyth, J. Nash, and J. Moum, Differential diffusion in breaking Kelvin-Helmholtz billows, *J. Phys. Oceanogr.* **35**, 1004 (2005).
- [44] P. F. Fischer, J. W. Kruse, Lottes, and S. Kerkemeier, NEK5000 webpage, <http://nek5000.mcs.anl.gov> (2008).

- [45] P. F. Fischer, An overlapping Schwarz method for spectral element solution of the incompressible Navier-Stokes equations, *J. Comput. Phys.* **133**, 84 (1997).
- [46] P. Fischer and J. Mullen, Filter-based stabilization of spectral element methods, *C. R. Acad. Sci., Ser. I, Math.* **332**, 265 (2001).
- [47] R. Furue, Energy transfer within the small-scale oceanic internal wave spectrum, *J. Phys. Oceanogr.* **33**, 267 (2003).
- [48] A. Nelson, B. Arbic, D. Menemenlis, W. Peltier, M. Alford, N. Grisouard, and J. Klymak, Improved internal wave spectral continuum in a regional ocean model, *J. Geophys. Res. Oceans* **125**, e2019JC015974 (2020).
- [49] Y. Pan, B. K. Arbic, A. D. Nelson, D. Menemenlis, W. Peltier, W. Xu, and Y. Li, Numerical investigation of mechanisms underlying oceanic internal gravity wave power-law spectra, *J. Phys. Oceanogr.* **50**, 2713 (2020).
- [50] P. Garaud, Double-diffusive convection at low Prandtl number, *Annu. Rev. Fluid Mech.* **50**, 275 (2018).
- [51] L. Padman and T. M. Dillon, Thermal microstructure and internal waves in the Canada Basin diffusive staircase, *Deep Sea Res. Part A* **36**, 531 (1989).
- [52] Y. Yang, R. Verzicco, D. Lohse, and C. Caulfield, Layering and vertical transport in sheared double-diffusive convection in the diffusive regime, *J. Fluid Mech.* **933**, A30 (2022).
- [53] D. E. Kelley, Fluxes through diffusive staircases: A new formulation, *J. Geophys. Res. Oceans* **95**, 3365 (1990).
- [54] T. Newell, Characteristics of a double-diffusive interface at high density stability ratios, *J. Fluid Mech.* **149**, 385 (1984).
- [55] M. G. Worster, Time-dependent fluxes across double-diffusive interfaces, *J. Fluid Mech.* **505**, 287 (2004).
- [56] M. E. Stern, Inequalities and variational principles in double-diffusive turbulence, *J. Fluid Mech.* **114**, 105 (1982).
- [57] G. O. Marmorino and D. R. Caldwell, Heat and salt transport through a diffusive thermohaline interface, in *Deep Sea Research and Oceanographic Abstracts*, Vol. 23 (Elsevier, Amsterdam, 1976), pp. 59–67.
- [58] W. G. Large, J. C. McWilliams, and S. C. Doney, Oceanic vertical mixing: A review and a model with a nonlocal boundary layer parameterization, *Rev. Geophys.* **32**, 363 (1994).